

Dorsal Amygdala Neurotrophin-3 Decreases Anxious Temperament in Primates

Andrew S. Fox, Tade Souzaiaia, Jonathan A. Oler, Rothem Kovner, Jae Mun (Hugo) Kim, Joseph Nguyen, Delores A. French, Marissa K. Riedel, Eva M. Fekete, Matthew R. Rabska, Miles E. Olsen, Ethan K. Brodsky, Andrew L. Alexander, Walter F. Block, Patrick H. Roseboom, James A. Knowles, and Ned H. Kalin

ABSTRACT

BACKGROUND: An early-life anxious temperament (AT) is a risk factor for the development of anxiety, depression, and comorbid substance abuse. We validated a nonhuman primate model of early-life AT and identified the dorsal amygdala as a core component of AT's neural circuit. Here, we combine RNA sequencing, viral-vector gene manipulation, functional brain imaging, and behavioral phenotyping to uncover AT's molecular substrates.

METHODS: In response to potential threat, AT and brain metabolism were assessed in 46 young rhesus monkeys. We identified AT-related transcripts using RNA-sequencing data from dorsal amygdala tissue (including central nucleus of the amygdala [Ce] and dorsal regions of the basal nucleus). Based on the results, we overexpressed the neurotrophin-3 gene, *NTF3*, in the dorsal amygdala using intraoperative magnetic resonance imaging-guided surgery ($n = 5$ per group).

RESULTS: This discovery-based approach identified AT-related alterations in the expression of well-established and novel genes, including an inverse association between *NTRK3* expression and AT. *NTRK3* is an interesting target because it is a relatively unexplored neurotrophic factor that modulates intracellular neuroplasticity pathways. Overexpression of the transcript for *NTRK3*'s endogenous ligand, *NTF3*, in the dorsal amygdala resulted in reduced AT and altered function in AT's neural circuit.

CONCLUSIONS: Together, these data implicate neurotrophin-3/*NTRK3* signaling in the dorsal amygdala in mediating primate anxiety. More generally, this approach provides an important step toward understanding the molecular underpinnings of early-life AT and will be useful in guiding the development of treatments to prevent the development of stress-related psychopathology.

Keywords: AAV, Amygdala, Anxiety, Anxious temperament, Behavioral inhibition, Central nucleus of the amygdala, Extended amygdala, FDG-PET, Neurotrophic, *NTF3*, *NTRK3*, Primate, RNA-seq

<https://doi.org/10.1016/j.biopsych.2019.06.022>

Anxious temperament (AT) early in life is a major risk factor for the later development of anxiety and depressive disorders along with comorbid substance abuse (1–3). Understanding the molecular alterations that give rise to extreme AT is an important step toward developing targeted behavioral and pharmacological treatments for early-life anxiety. Given our current understanding of these processes, it is critical to combine discovery-based approaches with interventions targeted to test novel molecular substrates to understand the relevance of the many molecular pathways associated with increased childhood anxiety (4). The rhesus monkey is an ideal species for translational research focused on the molecular underpinnings of AT. In addition to the remarkable similarities between young monkeys and children in the expression of AT, studies in rhesus monkeys allow for the combination of targeted mechanistic techniques with neuroimaging techniques commonly used in humans. Here, we take advantage of the recent

evolutionary divergence between humans and rhesus monkeys to identify putative molecular underpinnings of AT in the central nucleus (Ce)-containing dorsal amygdala region. These efforts combine in-depth phenotyping, including brain imaging and behavioral assessments, with postmortem RNA sequencing (RNA-seq) along with targeted viral-vector-mediated gene expression to test causality.

Neuroimaging studies of anxiety disorders and anxious dispositions performed in children (5), adults (6), and rhesus monkeys (7,8) reveal a brain-wide network of AT-related regions that encompasses portions of the extended amygdala, including the bed nucleus of the stria terminalis (BST) and the Ce (9). In primates, the Ce-containing dorsal amygdala strongly projects to the BST (10,11), is functionally connected with the rest of the extended amygdala (12,13), and is hypothesized to play a critical role in threat learning and processing (14,15). The dorsal amygdala receives direct and indirect projections from

regulatory and evaluative cortical regions, and within the dorsal amygdala, the Ce can initiate defensive behavioral and physiological responses via projections to downstream targets (14,15). The primate Ce has been causally implicated in AT (16,17) and dorsal amygdala metabolism is largely non-heritable, suggesting that the environmental factors affecting AT may be mediated by the dorsal amygdala (7,18). Here, we focused our efforts on understanding molecular alterations in the environmentally sensitive dorsal amygdala region that mediates AT.

Forty-six nonhuman primates were longitudinally assessed for behavioral inhibition, cortisol, and brain metabolism during a 30-minute exposure to a potentially threatening human intruder who made no eye contact (NEC) with the monkey. The NEC context elicits behavioral inhibition, which in children is a prominent risk factor for developing stress-related psychopathology. During NEC, we measured behavioral inhibition (freezing and vocal reductions) as well as plasma cortisol levels and combined them to create a composite measure of AT (7,8,18). To assess regional brain metabolism during NEC, animals were injected with 18-fluorodeoxyglucose (^{18}F FDG) immediately prior to the exposure to the NEC context, and integrated brain metabolism occurring during NEC was assessed using positron emission tomography (PET). The phenotyping and imaging data from 22 of the animals were previously presented and included initial gene expression studies using microarray techniques. Consistent with our previous work (19), AT was stable across repeated assessments (Figure 1A), and metabolism in the AT network, including the dorsal amygdala, was associated with increased AT (Figure 1B, Table S1 in Supplement 2, and Figure S1 in Supplement 1).

Tissue for RNA-seq was harvested from the dorsal amygdala region from the 46 animals that completed behavioral, endocrine, and brain metabolism assessments (Figure 1A–C). RNA-seq was performed using NuGEN Ovation RNA-seq v2 (Tecan Genomics, Redwood City, CA) libraries on Illumina DNA sequencers (San Diego, CA) with ~30 million 100-base pair reads per animal. Reads were mapped and quantified using an updated version of the RseqFlow pipeline (20) designed specifically for the rhesus monkey genome and transcriptome (UNMC Rhesus v7.6.8; University of Nebraska Medical Center, Omaha, NE) (21) and resulted in estimates of expression levels for each annotated exon, intron, and junction of each gene. Performing RNA-seq in these 46 animals allowed for the opportunity to replicate and extend earlier microarray-based findings generated from one half of these animals using a more in-depth approach (see Supplement 1; findings will be discussed separately when relevant).

METHODS AND MATERIALS

A summary of the methods and procedures most relevant to understanding the RNA-seq and adeno-associated virus (AAV)-NTF3 overexpression studies are provided below. Complete detailed methods can be found in Supplement 1, including FDG-PET and surgical details.

RNA-seq: Animals

In 46 young male periadolescent rhesus monkeys (mean age = 3.3 years), we examined Ce gene expression using RNA-seq in

combination with assessments of behavior, physiology, and functional brain imaging. AT was assessed in response to the potentially threatening NEC condition of the human intruder paradigm, using a composite of increased freezing, decreased vocalizations, and increased cortisol. Brain function was assessed using NEC-related ^{18}F FDG-PET. RNA-seq was performed using NuGEN Ovation RNA-seq v2 libraries on Illumina DNA sequencers with ~30 million 100-base pair reads per animal. Using regression techniques, we examined variation in Ce messenger RNA expression in relation to individual differences in AT, as well as structural and functional imaging measures. Because of the unique nature and difficulty of this approach, we sequenced RNA from a number of rhesus monkeys that had previously been examined using a microarray approach ($n = 22$, RNA-seq cohort 1) (19). The 22 animals that were a part of RNA-seq cohort 1 represent all animals discussed in Fox *et al.* (7) with sufficient RNA remaining to be sequenced. When relevant, we discuss these data separately from the 24 additional animals. The second cohort of 24 animals were completely new to this study (RNA-seq cohort 2); when relevant we discuss these animals separately. All procedures were approved by and in accordance with the guidelines established by the Institutional Animal Care and Use Committee at the University of Wisconsin—Madison.

RNA-seq: RNA Purification and Quantification

RNA-seq was performed using a modification of the SPIA reaction of the NuGEN Ovation RNA-seq v2 kit for cDNA Synthesis, followed by library construction using the NuGEN Rapid no-PCR protocol in a NuGEN Mondrian microfluidics instrument. RNA-seq libraries were then sequenced to a minimum depth of ~30 million single-end 101-base pair reads. RNA-seq reads were aligned to the Rhesus genome (MaSuRCA v7) using PerM as described in RseqFlow (20), and annotated using the rhesus transcriptome (UNMC v7.6.8). Reads that aligned to coding exons and known junctions in each gene model were summed and normalized (quantile and reads per kilobase million) to provide a raw proxy for gene expression.

RNA-seq: Statistical Analyses

Building on our previous work, we examined transcript features of each gene model, such as exons, introns, and splice junctions, in relation to AT in python using statsmodels (<https://github.com/statsmodels/statsmodels/>). Because annotation of the rhesus genome is ongoing, and our understanding of splice variation still developing, we performed gene-level multiple regression analyses to predict AT. Each multiple regression analysis was performed in 2 steps: 1) nuisance variable age was entered into the model to predict AT, and 2) estimated expression levels for each exon were simultaneously entered. The test of interest was the significance of the change in F between step 1 and step 2, which accounts for the variance explained by the exonic expression levels. The degrees of freedom for this model vary depending on the number of exons expressed for each gene. Analyses were restricted to genes where we mapped an average of at least 10 reads across

Dorsal Amygdala NT-3 Decreases AT in Primates

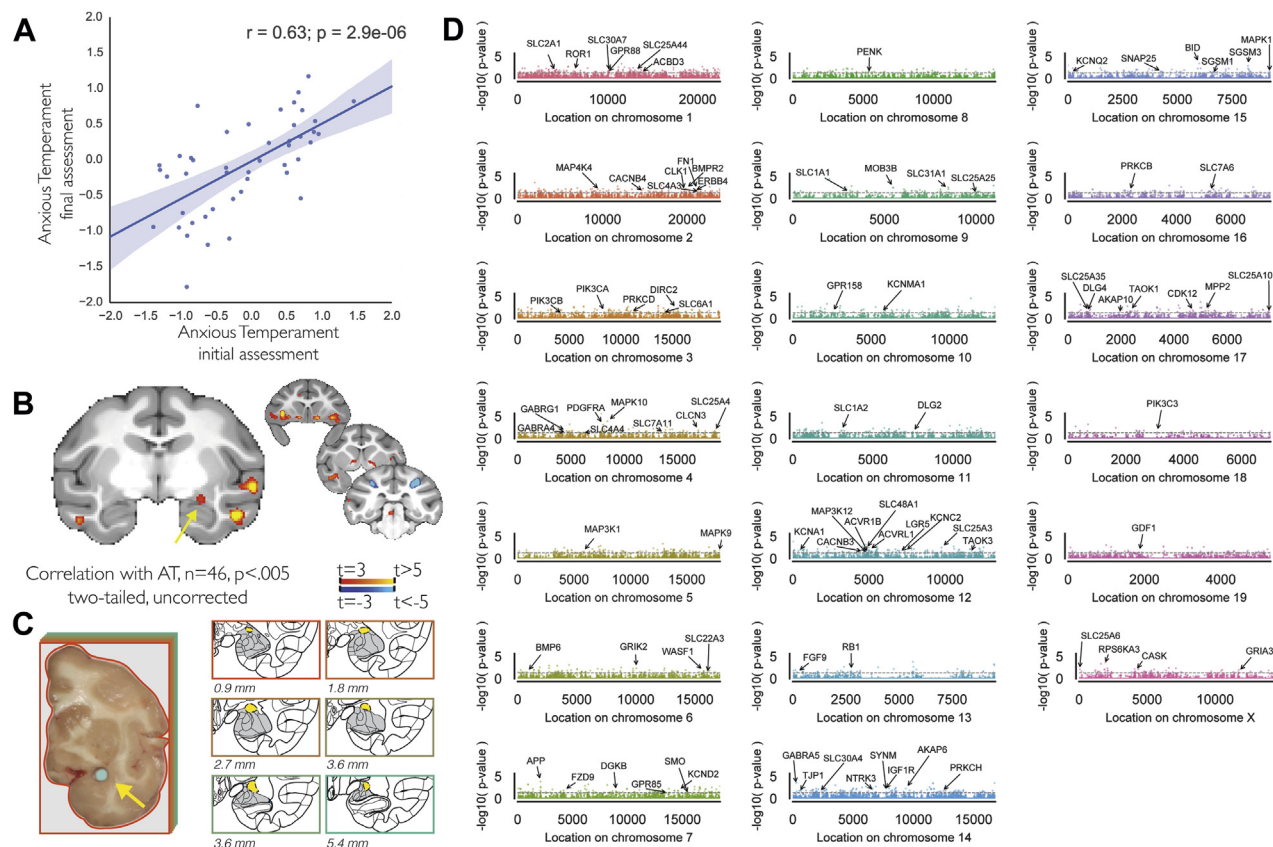


Figure 1. Anxious temperament (AT) is associated with a brain-wide AT network and altered gene expression in the dorsal amygdala. **(A)** Assessment of AT in 46 young male rhesus monkeys revealed AT to be stable over time ($r = .63$, $p < .001$). **(B)** Average AT across assessments was associated with metabolic changes in an AT-related brain network ($p < .005$, 2-tailed uncorrected), including the dorsal amygdala region (yellow arrow, also see Figure S1 in Supplement 1). **(C)** Dorsal amygdala tissue was harvested from these same animals (yellow arrow), RNA was extracted and mapped to the rhesus genome (MaSuRCA v7; UNMC v7.6.8), and a multiple regression was run for each gene with AT as the dependent variable and each exon's expression levels as the independent measure (see Methods and Materials for details). **(D)** Results demonstrated distributed associations between dorsal amygdala gene expression and AT across chromosomes, as can be seen in this Manhattan plot depicting the log-p value for the F test of all exons regressed against AT. Genes reaching $p < .05$ significance were annotated if they were a part of the Human Genome Organization gene families that included any of the following in its title: "G protein," "endogenous ligands," "kinases," "aminobutyric," "glutamate," "mitogen-activated," "channels," "SNAREs," "solute carrier."

rhesus monkeys, and at least 1 read in each animal. Additional follow-up analyses can be found in Supplement 1.

AAV5-NTF3: Animals

Thirty-five potential animals were behaviorally screened for participation in the NT3 viral-vector study with 10 minutes of the NEC condition, and 10 periadolescent male animals were selected (mean age at surgery = 2.43 ± 0.19 years). Selected animals displayed freezing in response to the NEC that ranged from 133.4 seconds to 377.5 seconds (of 600 seconds total). These animals were selected because they were in the mid-high range of freezing to maximize the likelihood of observing the hypothesized NT3-induced changes in AT.

All 10 animals were scanned with magnetic resonance imaging (MRI) and FDG-PET both before and after surgery (AAV5-NTF3 group) or rest (unoperated cage-mate control animals). Animals were first assessed using FDG-PET imaging an average of 48.9 ± 4.1 days prior to surgery. MRI data were collected roughly 2 weeks after the PET scan, averaging

33.6 ± 1.4 days prior to surgery. As in the RNA-seq animals, AT was assessed in response to the potentially threatening NEC condition of the human intruder paradigm, using a composite of increased freezing, decreased vocalizations, and increased cortisol, and brain function was assessed using NEC-related ^{18}F FDG-PET. An AAV5 viral vector designed to overexpress NTF3, the primary ligand for NTRK3, was injected into the dorsal amygdala region of 5 animals using real-time intraoperative surgeries. Animals were pair-housed, and 1 animal from each pair was randomly assigned to receive dorsal amygdala AAV5-NTF3 injections. Postsurgical FDG-PET scans were collected an average of 65.1 ± 6.4 days after surgery, allowing sufficient time for recovery. Postsurgical MRI scans were collected an average of 75.8 ± 5.1 days after the surgery. All statistical tests compared post- and prechange between dorsal amygdala AAV5-NTF3 animals and their cage-mate control animals. All procedures were approved by and in accordance with the guidelines established by the Institutional Animal Care and Use Committee.

AAV-NTF3: Viral Vector

The DNA sequence corresponding to the entire open reading frame of the rhesus *NTF3* (GenBank accession #XM_001118191, bases 8 to 1033; National Center for Biotechnology Information, Bethesda, MD) was inserted into the viral vector pAAV-MCS (Vector Biolabs, Malvern, PA). Neurotrophin-3 (NT-3) protein expression was confirmed (see the Supplemental Methods in Supplement 1 for details) and the plasmid was then packaged into rAAV5 (Vector Biolabs) with a titer of 1.2×10^{13} genome copies/mL.

AAV-NTF3: Statistical Analyses

Changes between pre- and postsurgical measures of AT were computed for the dorsal amygdala AAV5-*NTF3* animals and compared with similarly spaced assessments of the control animals. Corresponding comparisons were also performed to assess the effects of dorsal amygdala AAV5-*NTF3* on the components of AT, that is, freezing, cowering, and cortisol levels. The effects of *NTF3* overexpression were assessed using the statsmodels package in python. We also performed targeted and voxelwise analyses to examine the effects of *NTF3* overexpression on brain metabolism (see the Supplemental Methods in Supplement 1 for details). Briefly, we first computed the changes in metabolism pre- and postsurgery and for similarly timed assessments in control animals. We then performed group Student's *t* tests to compare changes in metabolism between groups. Exploratory voxelwise neuroimaging analysis results were thresholded at a liberal $p < .05$ 2-tailed, uncorrected.

Additional detailed methods can be found in Supplement 1.

RESULTS

RNA-seq of Dorsal Amygdala Tissue Reveals Many Genes With AT-Related Expression Levels

We first identified AT-related transcripts based on exon expression levels. Because annotation of the rhesus genome is ongoing, and our understanding of splice variation is still developing, we performed gene-level multiple regression analyses to predict AT, where expression levels for each exon within a gene were simultaneously entered into a regression model to predict AT, while controlling for age and sex. This approach is well suited for analysis of genomes with incomplete annotations that preclude a full splice-variant quantification. Additionally, this approach is not biased toward identifying well-annotated genes or genes with many exons (though it is limited by degrees of freedom in genes with >40 exons). Results demonstrated 67 genes to have AT-related exonic expression at $p < .005$ (2-tailed uncorrected) (Table S2 in Supplement 2), and 618 genes at a threshold $p < .05$ (2-tailed uncorrected) (Figure 1D; Table S2 in Supplement 2).

In addition to our primary analyses, we performed complementary analyses to identify AT-related dorsal amygdala transcripts, including examining various aspects of each gene's expression profile (e.g., quantifying each intron, exon, and junction independently, averaging expression across the whole gene, and mapping each gene to the human genome), performing gene enrichment analyses, and independently examining each component of AT at each assessment (i.e.,

freezing, cowering, cortisol, at first and last assessment) in relation to gene expression (see Methods and Materials section). To provide discovery opportunities to interested readers, all AT-related analyses, including post hoc complementary analyses, can be accessed via our web resource (<http://at.psychiatry.wisc.edu>; https://github.com/asfox/AT_DorsalAmygdala_RNAseq_FoxEtAl).

Results of our gene-level multiple regression approach demonstrated that a number of neuroplasticity-related molecules were inversely associated with AT, including the neurotrophic receptor, *NTRK3* (Figure 2A–B), and its downstream modulator *RPS6KA3* (Figure S2 in Supplement 1) (19). Other AT-related transcripts included the inhibitory neurotransmitter receptor subunit *GABRA5* (see Supplement 1 and Figure S3 in Supplement 1), *GABBR1*, and *APP* (Figure S4 in Supplement 1).

Pathway and Ontology Analyses Underscore the Importance of Neuroplasticity-related Processes in the Dorsal Amygdala Region as Important for AT

Consistent with our neurodevelopmental hypothesis (4), gene ontology and the Kyoto Encyclopedia of Genes and Genomics' KEGG PATHWAY (<https://www.genome.jp/kegg/pathway.html>) enrichment analyses of the 618 nominally significant AT-related genes revealed significant overrepresentation of genes in the neurotrophin signaling pathway (KEGG: hsa04722; $z = -1.73$, $p = .01884$) (additional significant pathways can be seen in Table S5 in Supplement 2), which includes one of the stronger hits in our dataset, the ribosomal protein *RPS6KA3*, a downstream kinase that can be modulated by tyrosine kinase (Trk)-receptor activation, which was associated with AT and each of its components (Figure S3 in Supplement 1). Moreover, we found overexpression in numerous plasticity-related categories, mammalian target of rapamycin signaling pathway (KEGG: hsa04150), negative regulation of apoptotic process (Gene Ontology identifier: GO:0043066), regulation of apoptotic process (GO:0042981), regulation of target of rapamycin signaling (GO:0032006), positive regulation of long-term synaptic potentiation (GO:1900273), and protein serine/threonine kinase activator activity (GO:0043539). Full tables of overexpression analyses can be seen in Tables S5 and S6 in Supplement 2. Additionally, we also found significant overrepresentation within other potentially AT-related ontology categories, including behavioral fear response (GO:0001662), regulation of translation in response to stress (GO:0043555), and Wnt signaling pathway (GO:0016055). Although the informatics tools for making these comparisons are still developing alongside our actual knowledge about these pathways, these results continue to support the relevance of multiple molecular contributors to AT and suggest that neuroplasticity-related factors may play an important role.

Post Hoc Analyses of RNA-seq of Dorsal Amygdala Tissue Support NTRK3 as a Reliable Target for AT-Related Alterations

Because of our interest in neuroplasticity as a protective factor for the development of anxiety disorders (4), and in the *NTRK3* pathway specifically, we present complementary post hoc analyses related to *NTRK3*. Importantly, the negative relation

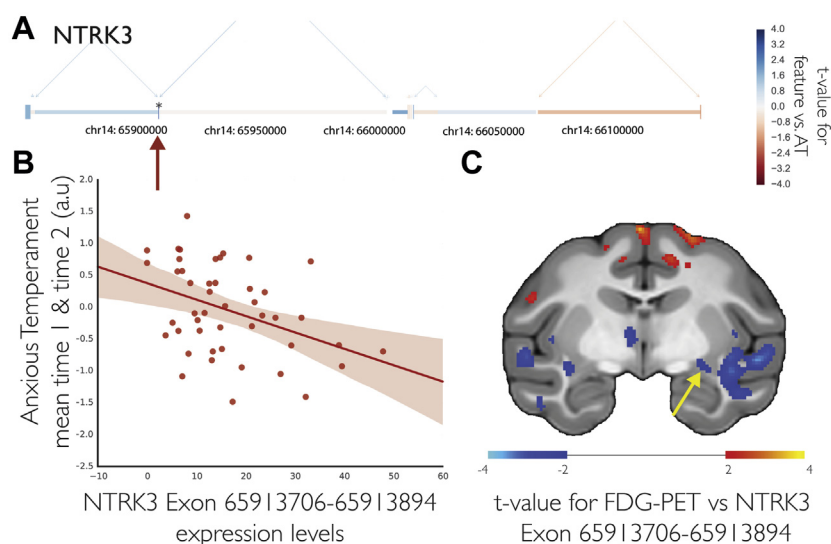


Figure 2. *NTRK3* expression is associated with anxious temperament (AT). *NTRK3* gene model with each exon colored by the *t* value of the association between that exon and AT in 46 young rhesus monkeys (A) shows exons between 65913706 and 65913894 to be inversely associated with AT (B). (C) *NTRK3* gene expression is associated with a distributed brain metabolic network ($p < .05$, 2-tailed uncorrected) including an inverse association with the dorsal amygdala region (yellow arrow). a.u., arbitrary unit; FDG-PET, fluorodeoxyglucose-positron emission tomography.

between *NTRK3* and AT was significant ($n = 24$, $t = -2.08$, $p = .0494$, $r = -.41$, 95% confidence interval [CI] = -0.58 , -0.22) when excluding the initial cohort, in which, using microarray technology, we previously identified a relationship between AT and *NTRK3*. This demonstrates independent replication of the inverse AT-*NTRK3* relationship (19). Next, we performed nonparametric analyses in the entire sample, encompassing both cohorts ($n = 46$), which revealed that AT was associated with whole-gene *NTRK3* expression levels ($n = 46$, $\rho = -.35$, $p = .019$, 95% CI = -0.47 , -0.22). Post hoc examination of individual *NTRK3* exon expression levels in relation to AT revealed only one exon to be significantly associated with AT on its own (exon coordinates: 65913706–65913894; $n = 46$, $t = -2.76$, $p = .009$, $r = -.38$, 95% CI = -0.5 , -0.25), suggesting that specific *NTRK3* isoforms may be uniquely associated with AT. Nonparametric Spearman's correlations across the entire sample revealed expression levels of additional *NTRK3* gene features along the full length of the gene to be significantly correlated with AT (3 of 7 exons, 0 of 8 introns, and 4 of 9 splice junctions; p 's $< .05$).

We then correlated expression levels at the most significant *NTRK3* exon with brain metabolism to determine whether *NTRK3* expression was associated with dorsal amygdala metabolism. More specifically, we performed a voxelwise search for regions where expression levels of this AT-related *NTRK3* exon was associated with FDG uptake during the NEC context. Results demonstrated dorsal amygdala expression of the most AT-related *NTRK3* exon to be inversely associated with metabolism in the dorsal amygdala region during NEC ($n = 46$, p 's $< .05$, uncorrected) (Figure 2C).

NT-3 Overexpression in Dorsal Amygdala Decreased AT and Altered Extended Amygdala Metabolism

Based on these data, we hypothesized that increased *NTRK3* signaling in dorsal amygdala would decrease AT. To test this

hypothesis, we used viral-vector techniques to increase activation of the *NTRK3* pathway via overexpression of its endogenous ligand NT-3. Using real-time intraoperative MRI, we infused an *AAV5-Cmv-NTF3* viral vector into the dorsal amygdala of 5 young rhesus monkeys and compared them with 5 unoperated control animals (Figure 3A–D; see Methods and Materials). Overexpression of *NTF3* in dorsal amygdala neurons resulted in a significant decrease in AT in rhesus monkeys compared with control animals ($n = 5$ /group; nonparametric Mann-Whitney $U = 4.0$, $p = .047$; parametric test was 2-tailed trend-level significant in the predicted direction both with unpaired, $t = -2.176$, $p = .061$, Cohen's $d = 1.54$ with 95% CI = -1.1 , 0.66 , and with paired groups, as the study was designed, $t = -2.515$, $p = .066$, Cohen's $d = -1.03$ with 95% CI = -2.16 , 0.11) (Figure 3F). Further inspection of the components of AT revealed a significant effect of dorsal amygdala *NTF3* overexpression in the predicted direction reducing threat-related freezing ($t = -3.013$, $p = .039$, Cohen's $d = -1.23$ with 95% CI = -2.36 , -0.1) (Figure 3F, right top). Though in the predicted direction, the post- and prechanges were not significant for cooing (though only 1 animal emitted a coo call during this experiment, $t = 1.000$, $p = .374$, Cohen's $d = 0.41$ with 95% CI = -0.72 , 1.54) (Figure 3F, right middle) or cortisol ($t = -0.693$, $p = .527$, Cohen's $d = -0.28$ with 95% CI = -1.42 , 0.85) (Figure 3F, right bottom). Because of the relatively large CI for point estimates and the relationships between *NTRK3* expression and the components of AT in the RNA-seq study, we choose not to interpret these differences in the overexpression study. Nevertheless, the results suggest that in order to produce maximal alterations of AT that affect all of AT's components, effective treatments may require multiple genetic targets. Although we do not interpret these null effects, follow-up analyses focused on freezing.

We predicted that dorsal amygdala *NTF3* overexpression would alter brain metabolism. We found a postsurgical increase in metabolism compared with control animals within the dorsal amygdala intraoperative MRI-defined infusion region

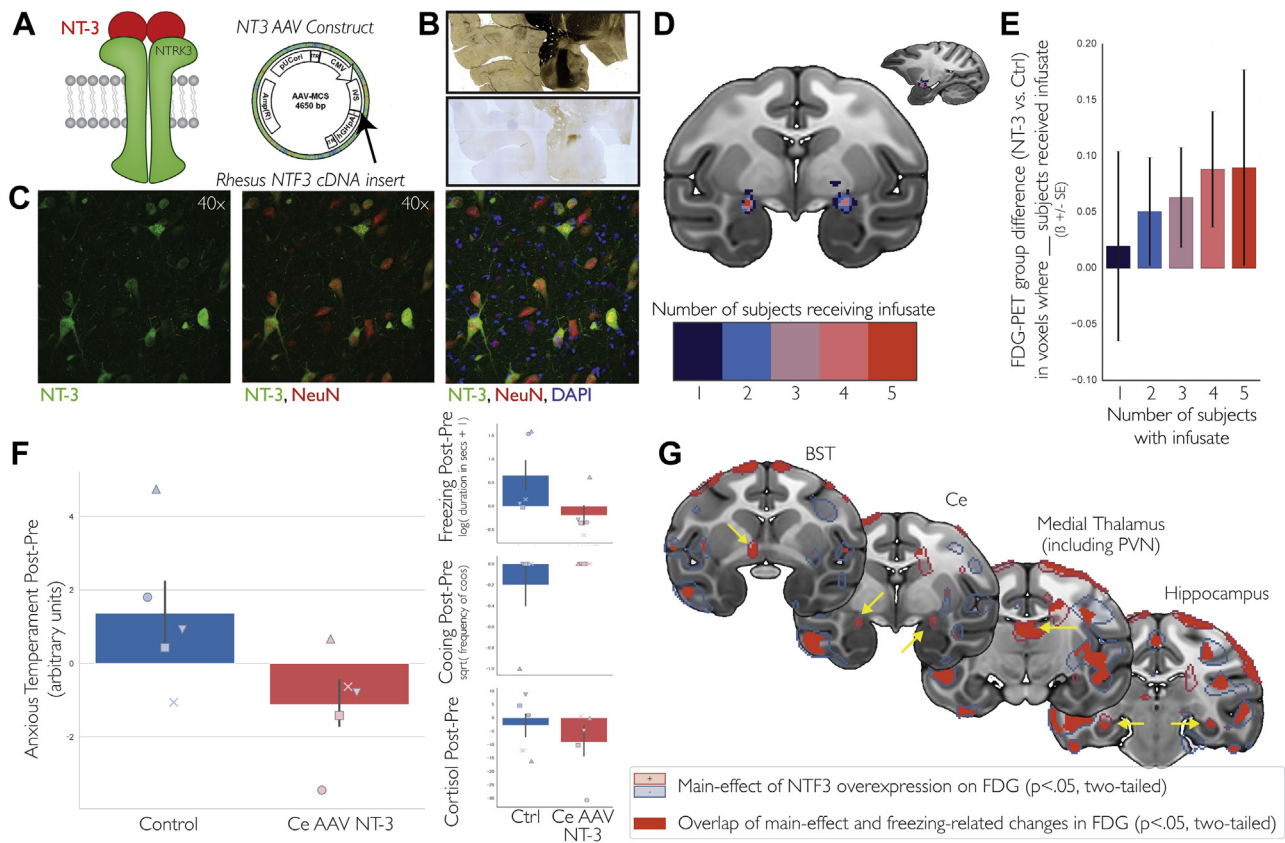


Figure 3. Adeno-associated virus (AAV)5-*NTF3* overexpression in the dorsal amygdala alters regional metabolism and decreases anxious temperament (AT). (A) Because neurotrophin-3 (NT-3) is the primary ligand for NTRK3 (left), we infused AAV5 containing the *NTF3* construct (right) to overexpress NT-3 in the dorsal amygdala of 5 young rhesus monkeys, using convection-enhanced delivery and intraoperative magnetic resonance imaging-guided surgical techniques (30,32). Expression of NT-3 was verified using precise postmortem dorsal amygdala localization using corresponding acetylcholinesterase staining (B, top) with an NT-3 antibody for visualization of overexpression (B, bottom), and high-magnification co-staining demonstrating selective neuronal expression: NT-3 (green), NeuN (red; neurons), and 4',6-diamidino-2-phenylindole (DAPI) (blue; cell nuclei) (C). We demonstrated accurate targeting of the infusate into bilateral dorsal amygdala region in all 5 animals after transformation to standard space (D), using premortem real-time T1-weighted magnetic resonance imaging of the viral-vector mixed with radiopaque Gd infusate. (E) Results demonstrated infusion-overlap-related group differences in no eye contact-context metabolism, such that the infusion-induced metabolic changes were larger in those voxels in which more monkeys received infusate ($n = 5$) compared with uninjected control (Ctrl) animals ($n = 5$). (F) AAV-*NTF3* infusion was associated with decreases in AT ($n = 5$ /group) (left). Dorsal amygdala AAV-*NTF3* overexpression was significantly associated with decreased freezing but did not reach significance with cooling and cortisol (though in the predicted direction), suggesting that these changes could be specifically associated with freezing (right inset). Each central nucleus (Ce)-AAV-*NTF3* animal has its own marker, which is shared by its matched control animal. (G) Finally, we identified brain-wide metabolic changes that demonstrated a main effect of AAV-*NTF3* overexpression ($p < .05$, uncorrected; $n = 5$ /group), where changes in metabolism were correlated with changes in freezing across groups (red; $n = 10$) in regions that included the bed nucleus of the stria terminalis (BST), dorsal amygdala, medial thalamus, and hippocampus (yellow arrows). These data suggest that the behavioral alterations resulting from dorsal amygdala *NTF3* overexpression may be mediated by a distributed network of metabolic changes. cDNA, complementary DNA; FDG-PET, fluorodeoxyglucose-positron emission tomography; PVN, paraventricular nucleus.

(Figure 3E). Voxelwise analyses identified *NTF3*-induced freezing-related metabolic changes within the AT network (Figure 3G and Tables S3 and S4 in Supplement 2). These regions, which are likely to mediate the effects of *NTF3* on AT, included the Ce region and BST region, as well as regions of the medial thalamus and hippocampus. Interestingly, we found that the metabolic alterations in these regions, which are normally positively associated with AT and freezing behavior, were inversely associated with the *NTF3*-related change in freezing. This unexpected finding highlights the important and interesting disconnect between unitary measures of brain activity and the complex molecular systems that give rise to

variation in brain function. Taken together, these findings suggest that neuroplasticity in the dorsal amygdala modulates the function of the distributed neural circuit underlying anxiety.

DISCUSSION

Here, in a highly relevant AT-nonhuman primate model, we found variation in dorsal amygdala *NTRK3* expression levels to be inversely associated with AT. Importantly, overexpression of NT-3, the major NTRK3-activating ligand, was sufficient to decrease AT. NTRK3, also known as TrkC, is a growth factor receptor located on the surface of the cell, having the potential

to alter neuron growth and synaptic plasticity via the intracellular signaling pathways it shares with other Trk receptors (22,23). The current results implicate a novel translationally relevant neurotrophic pathway within the primate dorsal amygdala, which complements studies implicating other neurotrophic factors such as BDNF (brain-derived neurotrophic factor) and FGF2 (basic fibroblast growth factor) in rodent models of anxiety (24–26). The data presented here support our hypothesis implicating altered dorsal amygdala neuroplasticity as a molecular substrate for the early-life risk to develop anxiety and depressive disorders.

Additional in-depth in vitro and in vivo studies will be important to elucidate the effects of NTRK3 pathway activation at microcircuit and molecular levels. For example, we found that *NTF3* overexpression resulted in both a decrease in AT and an increase in metabolism throughout AT-related regions, which included the Ce-containing dorsal amygdala region and the Ce-projecting BST region. This finding contrasts with our previous work in a large sample of 592 rhesus monkeys that identified AT-related metabolism in these same regions to be positively correlated with AT. It is interesting that we did not observe a positive correlation between AT and aggregate Ce metabolism after *NTF3* overexpression. Perhaps this is not surprising, as these data lend important insight into our previous observation that only a small amount of the variability in AT could be accounted for by regional metabolism during NEC (7). Studies in rodents suggest that within regions as small as a typical neuroimaging voxel there often are neurons that produce opposing effects, as is the case with regard to mutually inhibitory populations within intra-Ce circuits (27). This emphasizes the importance of using preclinical models in conjunction with in vivo neuroimaging to understand the relationship between function at a microcircuit level with that represented in a single imaging voxel (14,27,28). The disparity in the direction of the effect provides potential insights into why many neuroimaging-phenotype associations typically explain relatively small amounts of variation. We believe, however, that these relatively weak associations do not detract from the importance of identifying regions using neuroimaging. In fact, it is likely that systems- and molecular-level studies can complement clinical neuroimaging and explain the variance that is unaccounted for by the aggregate signal in voxelwise neuroimaging measures (29). Here, at the molecular level, the precise mechanisms by which NT-3 or NTRK3 variation leads to alterations in metabolism and AT remain to be explored. For example, NT-3, like brain-derived neurotrophic factor, can also bind to NTRK2 (also known as tropomyosin receptor kinase B [TrkB]). Although not observed in the RNA-seq analyses, this raises the possibility that the NTRK2 pathway may also modulate AT in primates (23). We also emphasize that further studies focused on *NTRK3* isoforms are warranted, because in vitro studies demonstrate that NT-3 differentially interacts with NTRK3 receptor variants (23).

While we causally implicate the NT-3/NTRK3 system in AT, we emphasize that this target was but one of the many discovery-based associations. We have focused on

neuroplasticity-related signaling and the NT-3 system, but this is only one of many potential hypotheses that can be derived from the discovery-based RNA-seq data. Our RNA-seq analyses did not reveal results that survive strict multiple comparison correction and accordingly should be interpreted as moderate evidence in support of a particular molecule's involvement in anxiety. Nevertheless, there is much to be gleaned from further examination of AT-related transcripts on our online resource (<http://at.psychiatry.wisc.edu>, or https://github.com/asfox/AT_DorsalAmygdala_RNAseq_FoxEtAl), as there are many other dorsal amygdala transcripts that are associated with AT and/or distributed brain metabolism (e.g., Figures S2–S4 in Supplement 1). In addition to the findings presented here, it is likely that other anxiety-related gene expression relationships are being masked by incomplete and ongoing annotation of the rhesus genome. In addition to implicating the NT-3/NTRK3 system in the risk to develop anxiety and depressive disorders, these data underscore the importance of understanding the interactions among multiple molecular mechanisms that likely converge to influence the distributed neural network that underlies anxiety.

The demonstration that AT is decreased by dorsal amygdala *NTF3* overexpression complements our previous report of increased AT after overexpression of the *CRH* gene, which is associated with anxiety, in the dorsal amygdala (30). The *NTF3* and *CRH* overexpression studies were performed in independent samples, confirming that alterations in dorsal amygdala gene expression can bidirectionally change AT. From a methodological perspective, concerns regarding possible nonspecific effects of the surgery or infusions are mitigated by the demonstration that nearly identical methods were used in these two experiments that produced opposite but predicted behavioral effects. The mechanisms by which NT-3 and *CRH* overexpression result in opposing effects remains unknown. Rodent studies using Ce-CRH knockouts and optogenetic manipulation of Ce-CRH-expressing cells suggest that CRH may provide “gain control” on potentially threatening inputs (14,27,31). Previous research on growth factors suggests that the influence of NT-3 is unlikely to be that specific. Instead, it is more likely that NT-3 is exerting its influence on Ce function by altering the structural properties of Ce cells and altering synapses, including those to and from Ce-inhibitory interneurons, some of which are CRH positive. Additional research will be required to understand the overlap between CRH- and NTRK3-expressing cells, but it would be reasonable to hypothesize that effects of NT-3 increase local inhibition of CRH and other sets of peptide-expressing cells.

We identified potential molecular targets for the treatment and prevention of anxiety and depressive disorder and demonstrated causal manipulation of the NT-3/NTRK3 system in early-life AT. Identifying AT-related molecular alterations will provide new insights into the cell states and physiological features of the dorsal amygdala that are altered in highly anxious individuals. Such work promises to guide the development of new treatments for preventing and alleviating the lifelong suffering associated with stress-related psychopathology.

ACKNOWLEDGMENTS AND DISCLOSURES

This work was supported by Grant Nos. R01-MH046729 and R01-MH081884 (to NHK), as well as grants to National Primate Center Research Centers (Grant Nos. P51-OD011106 and P51-OD011107), and the Waisman Center (Grant No. P30-HD003352).

ASF and NHK conceptualized the study. NHK and ASF oversaw the study. TS mapped and quantified the RNA-seq data. ASF and JAO analyzed the brain-imaging data. ASF performed all across-animal statistical analyses. ASF, RK, and PHR analyzed the viral-vector infusion data. JAO, MR, EF, MRR, MEO, and EKB performed surgeries. DAF performed RNA extractions and viral-vector construction. MR, EF, and MRR assisted in data collection. ALA, WFB, and EKB contributed surgical analytic tools. ALA oversaw MRI collection. JAK oversaw RNA-seq and data analysis. JM(H)K performed library construction. ASF and NHK wrote the paper. All authors provided feedback.

We thank the personnel of the Harlow Center for Biological Psychology, the HealthEmotions Research Institute, the Waisman Laboratory for Brain Imaging and Behavior, the Wisconsin National Primate Research Center, the Wisconsin Institutes for Medical Research, A. Shackman, L. Williams, M. Jesson, D.P.M. Tromp, S. Shelton, and H. Van Valkenberg. We would also like to thank the University of California, Davis and the California National Primate Research Center for their support.

NHK has received honoraria from CME Outfitters, Elsevier, and the Pritzker Consortium; has served on scientific advisory boards for Actify Neurotherapies and Neuronetics; currently serves as an advisor to the Pritzker Neuroscience Consortium and consultant to Corcept Therapeutics; has served as co-editor of *Psychoneuroendocrinology* and currently serves as Editor-in-Chief of *The American Journal of Psychiatry*; and has patents on promoter sequences for corticotropin-releasing factor CRF2 α and a method of identifying agents that alter the activity of the promoter sequences (7,071,323; 7,531,356), promoter sequences for urocortin II and the use thereof (7,087,385), and promoter sequences for corticotropin-releasing factor binding protein and the use thereof (7,122,650). All other authors report no biomedical financial interests or potential conflicts of interest.

ARTICLE INFORMATION

From the Department of Psychology and the California National Primate Research Center (ASF), University of California, Davis, Davis, California; Department of Cell Biology (TS, JM(H)K, JN, JAK), Downstate Medical Center, State University of New York, Brooklyn, New York; Department of Psychiatry and the HealthEmotions Research Institute (JAO, RK, DAF, MKR, EMF, MRR, MEO, PHR, NHK) and Department of Medical Physics (EKB, ALA, WFB), University of Wisconsin–Madison, Madison, Wisconsin.

ASF and TS contributed equally to this work.

Address correspondence to Andrew S. Fox, Ph.D., 1 Shields Avenue, Department of Psychology, California National Primate Research Center, University of California, Davis, Davis, CA 95616; E-mail: dfox@ucdavis.edu or Ned H. Kalin, M.D., 6001 Research Park Blvd, Department of Psychiatry, University of Wisconsin–Madison, Madison, WI 53719; E-mail: nkalin@wisc.edu.

Received May 13, 2019; revised Jun 18, 2019; accepted Jun 25, 2019.

Supplementary material cited in this article is available online at <https://doi.org/10.1016/j.biopsych.2019.06.022>.

REFERENCES

- Biederman J, Hirshfeld-Becker DR, Rosenbaum JF, Herot C, Friedman D, Snidman N, *et al.* (2001): Further evidence of association between behavioral inhibition and social anxiety in children. *Am J Psychiatry* 158:1673–1679.
- Clauss JA, Blackford JU (2012): Behavioral inhibition and risk for developing social anxiety disorder: a meta-analytic study. *J Am Acad Child Adolesc Psychiatry* 51:1066–1075.e1.
- Essex MJ, Klein MH, Slattery MJ, Goldsmith HH, Kalin NH (2010): Early risk factors and developmental pathways to chronic high inhibition and social anxiety disorder in adolescence. *Am J Psychiatry* 167:40–46.
- Fox AS, Kalin NH (2014): A translational neuroscience approach to understanding the development of social anxiety disorder and its pathophysiology. *Am J Psychiatry* 171:1162–1173.
- Williams LE, Oler JA, Fox AS, McFarlin DR, Rogers GM, Jesson MA, *et al.* (2015): Fear of the unknown: uncertain anticipation reveals amygdala alterations in childhood anxiety disorders. *Neuropsychopharmacology* 40:1428–1435.
- Etkin A, Wager TD (2007): Functional neuroimaging of anxiety: a meta-analysis of emotional processing in PTSD, social anxiety disorder, and specific phobia. *Am J Psychiatry* 164:1476–1488.
- Fox AS, Oler JA, Shackman AJ, Shelton SE, Raveendran M, McKay DR, *et al.* (2015): Intergenerational neural mediators of early-life anxious temperament. *Proc Natl Acad Sci U S A* 112:9118–9122.
- Fox AS, Shelton SE, Oakes TR, Davidson RJ, Kalin NH (2008): Trait-like brain activity during adolescence predicts anxious temperament in primates. *PLoS ONE* 3:e2570.
- Shackman AJ, Tromp DPM, Stockbridge MD, Kaplan CM, Tillman RM, Fox AS (2016): Dispositional negativity: an integrative psychological and neurobiological perspective. *Psychol Bull* 142:1275–1314.
- de Olmos JS, Heimer L (1999): The concepts of the ventral striato-pallidal system and extended amygdala. In: McGinty JF, editor. *Advancing from the ventral striatum to the extended amygdala: Implications for neuropsychiatry and drug abuse*. New York: The New York Academy of Sciences, 1–32.
- Oler JA, Tromp DP, Fox AS, Kovner R, Davidson RJ, Alexander AL, *et al.* (2017): Connectivity between the central nucleus of the amygdala and the bed nucleus of the stria terminalis in the non-human primate: neuronal tract tracing and developmental neuroimaging studies. *Brain Struct Funct* 222:21–39.
- Oler JA, Birn RM, Patriat R, Fox AS, Shelton SE, Burghy CA, *et al.* (2012): Evidence for coordinated functional activity within the extended amygdala of non-human and human primates. *Neuroimage* 61:1059–1066.
- Tillman RM, Stockbridge MD, Nacewicz BM, Torrisi S, Fox AS, Smith JF, *et al.* (2018): Intrinsic functional connectivity of the central extended amygdala. *Hum Brain Mapp* 39:1291–1312.
- Fadok JP, Markovic M, Tovote P, Luthi A (2018): New perspectives on central amygdala function. *Curr Opin Neurobiol* 49:141–147.
- Fox AS, Oler JA, Tromp do PM, Fudge JL, Kalin NH (2015): Extending the amygdala in theories of threat processing. *Trends Neurosci* 38:319–329.
- Kalin NH, Shelton SE, Davidson RJ (2004): The role of the central nucleus of the amygdala in mediating fear and anxiety in the primate. *J Neurosci* 24:5506–5515.
- Oler JA, Fox AS, Shackman AJ, Kalin NH (2016): The central nucleus of the amygdala is a critical substrate for individual differences in anxiety. In: Amaral DG, Adolphs R, editors. *Living Without an Amygdala*. New York: Guilford Press, 218–251.
- Oler JA, Fox AS, Shelton SE, Rogers J, Dyer TD, Davidson RJ, *et al.* (2010): Amygdalar and hippocampal substrates of anxious temperament differ in their heritability. *Nature* 466:864–868.
- Fox AS, Oler JA, Shelton SE, Nanda SA, Davidson RJ, Roseboom PH, *et al.* (2012): Central amygdala nucleus (Ce) gene expression linked to increased trait-like Ce metabolism and anxious temperament in young primates. *Proc Natl Acad Sci U S A* 109:18108–18113.
- Wang Y, Mehta G, Mayani R, Lu J, Souaiaia T, Chen Y, *et al.* (2011): RseqFlow: workflows for RNA-Seq data analysis. *Bioinformatics* 27:2598–2600.
- Zimin AV, Cornish AS, Maudhoo MD, Gibbs RM, Zhang X, Pandey S, *et al.* (2014): A new rhesus macaque assembly and annotation for next-generation sequencing analyses. *Biol Direct* 9:20.
- Lamballe F, Klein R, Barbacid M (1991): trkC, a new member of the trk family of tyrosine protein kinases, is a receptor for neurotrophin-3. *Cell* 66:967–979.
- Martinowich K, Manji H, Lu B (2007): New insights into BDNF function in depression and anxiety. *Nat Neurosci* 10:1089–1093.
- Perez JA, Clinton SM, Turner CA, Watson SJ, Akil H (2009): A new role for FGF2 as an endogenous inhibitor of anxiety. *J Neurosci* 29:6379–6387.
- Song M, Martinowich K, Lee FS (2017): BDNF at the synapse: why location matters. *Mol Psychiatry* 22:1370–1375.
- Turner CA, Clinton SM, Thompson RC, Watson SJ Jr, Akil H (2011): Fibroblast growth factor-2 (FGF2) augmentation early in life alters

Dorsal Amygdala NT-3 Decreases AT in Primates

- hippocampal development and rescues the anxiety phenotype in vulnerable animals. *Proc Natl Acad Sci U S A* 108:8021–8025.
27. Fadok JP, Krabbe S, Markovic M, Courtin J, Xu C, Massi L, *et al.* (2017): A competitive inhibitory circuit for selection of active and passive fear responses. *Nature* 542:96–100.
28. Tye KM, Prakash R, Kim SY, Fenno LE, Grosenick L, Zarabi H, *et al.* (2011): Amygdala circuitry mediating reversible and bidirectional control of anxiety. *Nature* 471:358–362.
29. Fox AS, Shackman AJ (2019): The central extended amygdala in fear and anxiety: closing the gap between mechanistic and neuroimaging research. *Neurosci Lett* 693:58–67.
30. Kalin NH, Fox AS, Kovner R, Riedel MK, Fekete EM, Roseboom PH, *et al.* (2016): Overexpressing corticotropin-releasing hormone in the primate amygdala increases anxious temperament and alters its neural circuit. *Biol Psychiatry* 80:345–355.
31. Sanford CA, Soden ME, Baird MA, Miller SM, Schulkin J, Palmiter RD, *et al.* (2017): A central amygdala CRF circuit facilitates learning about weak threats. *Neuron* 93:164–178.
32. Emborg ME, Joers V, Fisher R, Brunner K, Carter V, Ross C, *et al.* (2010): Intraoperative intracerebral MRI-guided navigation for accurate targeting in nonhuman primates. *Cell Transplant* 19:1587–1597.

Dorsal Amygdala Neurotrophin-3 Decreases Anxious Temperament in Primates

Supplement 1

Table of Contents:

Supplemental Discussion: pg. 2-4

Supplemental Methods: pg. 4-21

Supplemental Figures: pg. 22-25

Supplemental References: pg. 26-28

Supplementary Discussion

RNA-seq analyses to discovery other AT-related transcripts

Although our focus was on *NTRK3*, this approach also served to implicate molecules that have long been hypothesized to underlie anxiety in the risk to develop anxiety and depressive disorders, and discover new potentially AT-related molecules that currently have no known role in anxiety. For example, significant AT-related transcripts included the inhibitory neurotransmitter receptor subunit, *gamma-aminobutyric acid (GABA) A receptor, alpha 5* (*GABRA5*, Figure S3), and the Alzheimer's associated *amyloid precursor protein* (*APP*; Figure S4). For example, post-hoc investigation of *APP* revealed that 8 different features were significant at $p < .005$ uncorrected, most of which were clustered at the A-Beta coding end of the transcript (1) (Figure S4).

In support of its hypothesized role in anxiety and anxiety-like behavior, we found an inverse relationship between AT and expression levels of *GABRA5*, which encodes the alpha-5 subunit of the GABA-A receptor. Ce *GABRA5* expression levels are known to be increased in highly anxious mice (2) and decrease after fear conditioning (3), a finding that is accompanied by decreased binding of benzodiazepines, a class of drugs often used to treat anxiety. It has previously been shown that genetic variation influencing expression of this gene has been associated with the anxiolytic response to benzodiazepines (4). And, recent work has demonstrated that, in specific populations of Ce neurons, alpha-5 containing GABA-A receptor complexes mediate the extrasynaptic tonic inhibition that underlies fear generalization (5). These findings are consistent

with the hypothesis put forth by Botta et al. (2015) (5) that experience-dependent changes in the expression of *GABAR5* contribute to anxiety by altering the signal-to-noise ratio of phasic fear-relevant inputs to Ce. The data presented here suggest that these specific aspects of *GABAR5* may be conserved in primate species, and related to the early-life risk factors for the development of anxiety and depressive disorders.

This discovery-based approach can also be used to identify AT-related expression levels of transcripts that have not previously been demonstrated to be anxiety-related. For example, we identified amyloid precursor protein (*APP*) as inversely associated with AT. *APP* is most frequently associated with Alzheimer's disease and the accumulation of amyloid deposits that result from cleaving the A β portion of the *APP* gene (6). Examination of the portions of the gene that were predictive of AT revealed that it was specifically the A β coding portion of the gene that was associated with AT (1). Cleavage products of the A β protein can regulate neuronal function and synaptic plasticity (7). Recent evidence suggests that portions of the APP protein bind to a specific sub-component of the metabotropic GABA type B receptor (GABBR1), which was also found to significantly predict AT in our dataset ($p=.037$; see Table S2). Our APP-GABA_BR1a data suggest the normative function of *APP* within the Ce may play a role in the neural instantiation of dispositional anxiety. These examples highlight the utility of this discovery-based approach, but ultimately mechanistic studies that demonstrate causality will determine their success.

In addition to these transcripts, many others could be of potential interest. To further explore the relationship between relevant AT-related transcripts and AT-related metabolism, we

correlated AT-related exon expression in genes of interest with metabolism throughout the AT circuit. These exploratory analyses revealed brain metabolism distributed throughout the AT-network to be associated with expression of various AT-related genes (see <http://at.psychiatry.wisc.edu>, or https://github.com/asfox/AT_DorsalAmygdala_RNAseq_FoxEtAl, along with some additional analyses of potential interest and <https://www.neurovault.org/collections/AYJGSCJH/>).

Supplementary Methods

Method details are broken down by technique as applied in the manuscript.

NEC-FDG: Assessing brain metabolism and AT (and its components) in the NEC context

Individual differences in the anxious temperament (AT) phenotype were quantified using the 30-minute No-Eye-Contact (NEC) condition of the human intruder paradigm (8-10). Subjects were placed in a testing cage, and an experimenter entered the room and stood motionless ~2.5 meters from the subject while presenting his profile and avoiding direct eye contact. Subjects were allowed to freely respond to this ethologically-relevant potential threat, similar to procedures used to assess children's dispositional anxiety and behavioral inhibition in response to a stranger. Anxiety-related behaviors elicited by the NEC challenge were scored by a trained rater, who was blind to monkey group assignment. Freezing was defined as a lack of movement for greater than 3-seconds, and was recorded in seconds / 5-minute epoch of NEC exposure. Mean freezing scores were log-transformed and converted to z-scores. Cooing was measured as the number of coo-vocalizations during each 5-minute epoch of NEC-exposure. Mean cooing frequencies were square-root transformed and converted to z-scores. For the RNA-seq study, but not the NT3-AAV study, freezing and cooing were standardized after covarying for age. This residualization was

not performed for the NT3-AAV study, because we were concerned it would induce more noise as a result of parameter instability, instead we selected animals that were the same age. Plasma cortisol ($\mu\text{g/dL}$) was quantified based on samples taken immediately after NEC-exposure. Plasma samples collected from animals used in the RNA-seq analysis were assayed for cortisol in duplicate using the DPC Coat-a-count radioimmunoassay (Siemens, Los Angeles, CA). The intra-assay CV% was 4.0 and the inter-assay CV% was 7.0. The limit of detection defined by the lowest standard was 1 $\mu\text{g/dL}$. The Siemens kit was subsequently discontinued; therefore, plasma samples collected from animals used in the NTF3 viral vector studies were assayed for cortisol in duplicate using the MP Biomedicals (Solon, OH) Immuchem coated tube radioimmunoassay. The intra-assay CV% was 4.9 and the inter-assay CV% was 10.3. The detection limit defined by the lowest standard was 1 $\mu\text{g/dL}$. In the RNA-seq data, cortisol values were standardized after removing any effects of age, and the time-of-day in which samples were taken. Similar to the behaviors described above, in the NT3-AAV study, cortisol values were not residualized. A composite measure of AT was computed as the average of standardized freezing, cooing and cortisol measures ($(Z_{\text{freezing}} - Z_{\text{cooing}} + Z_{\text{cortisol}}) / 3$). This was done across assessments for measures with multiple time-points. Further details on the validation and methods used to assess AT has been previously described (8, 11-13).

In order to measure threat-related metabolic activity animals were restrained in a squeeze cage, intravenously injected with FDG (~ 7.0 mCi), and then placed in a test cage for 30 minutes, during which time the animals were exposed to NEC. After the 30-minute FDG uptake period, animals were anesthetized with 15 mg/kg of ketamine and 0.04 mg/kg atropine and fitted with an endotracheal tube to maintain isofluorane (1-2%) anesthesia throughout the scanning procedure. Vital signs, including heart rate, oxygen saturation, end tidal CO_2 , respiration rate and body temperature, were monitored throughout the scan. RNA sequencing cohorts 1 and 2 were

scanned on a Concorde Microsystems P4 small animal microPET scanner (Siemens, Knoxville, TN) and the NT3 Viral Vector sample was scanned on the Siemens Focus220 microPET scanner. Sixty-minute emission PET scans were reconstructed using standard filtered back projection methods with attenuation- and scatter-correction, and reflect the integrated brain metabolism that occurred during the 30 minutes of FDG uptake. Each native-space FDG-PET image was linearly aligned to its corresponding T1 using a rigid-body transformation in ANTS (14, 15) and then aligned to the 592-monkey template using the T1 to template transformation. The normalized FDG-PET images were scaled to the whole-brain signal using FSL. The grand-mean scaled post-surgical PET images were subtracted from pre-surgical scaled PET images and then all scaled pre, post, post-pre PET images were spatially smoothed with a 4-mm FWHM Gaussian kernel.

MRI acquisition

Prior to MRI acquisition, the monkeys were anesthetized with ketamine (15 mg/kg, IM). The animals were placed in a MRI-compatible stereotaxic frame, administered dexmedetomidine (0.015 mg/kg, IM), and scanned for approximately one hour. Heart rate and oxygen saturation were monitored throughout the scan. Additional doses of ketamine were given as needed throughout the scan to maintain anesthesia. At the end of the scan the dexmedetomidine was reversed with atipamezole (0.15 mg/kg, IM) and animals were removed from the scanner and monitored until they fully recovered from anesthesia.

T1-weighted MRI scans, which were used for across subject registration, were adjusted for the three different cohorts, as seen below.

RNA sequencing cohort 1: Magnetic resonance imaging (MRI) was performed in a 3-Tesla GE Signa EXCITE (GE Healthcare; Waukesha, WI) scanner with a 16-cm quadrature extremity surface coil at the Waisman Laboratory for Brain Imaging and Behavior, in Madison, WI. The head was fixed in the sphinx position using a custom stereotaxic frame. Whole-brain anatomical images were acquired using a T1-weighted Enhanced Fast Gradient Echo 3-Dimensional (efgre3D, with inversion time [TI] = 600 ms, repetition time [TR] = 8.65 ms, echo time [TE] = 1.89 ms, flip angle = 10°, number of excitations [NEX] = 2, field of view [FOV] = 140 mm, matrix = 256 × 224, in-plane resolution = 0.27 mm, slice thickness = 1.0 mm, Spacing Between Slices = 0.5 mm, 248 slices).

RNA sequencing cohort 2: MRI was performed in a 3-Tesla GE DISCOVERY MR750 (GE Healthcare; Waukesha, WI) scanner with a 16-cm quadrature extremity surface coil at the Lane Imaging Laboratory at the HealthEmotions Research Institute (HERI), in Madison, WI. The head was fixed in the sphinx position using a custom stereotaxic frame. Whole-brain anatomical images were acquired using a coronal T1-weighted 3D Fast Spoiled Grass Sequence with IR Preparation (IR-FSPGR, with inversion time [TI] = 600 ms, repetition time [TR] = 11.45 ms, echo time [TE] = 5.4 ms, flip angle = 10°, number of excitations [NEX] = 2, field of view [FOV] = 140 mm, matrix = 256 × 224, in-plane resolution = 0.27 mm, slice thickness = 1.0 mm, Spacing Between Slices = 0.5 mm, 248 slices).

NT3 viral vector sample: MRI was performed in a 3-Tesla GE DISCOVERY MR750 (GE Healthcare; Waukesha, WI) scanner with a custom 8-channel array coil (Clinical MR Solutions; Brookfield, WI, USA) at the Lane Imaging Laboratory at the HERI, in Madison, WI. The head was fixed in the sphinx position using a custom stereotaxic frame that fit inside the coil. Whole-brain anatomical images were acquired using a coronal T1-weighted 3D Fast Spoiled Grass Sequence with IR Preparation (IR-FSPGR, with inversion time [TI] = 600 ms, repetition time [TR] = 11.92 ms, echo time [TE] = 5.4 ms, flip angle = 10°, number of excitations [NEX] = 2, field of view [FOV] = 140 mm, matrix = 256 × 224, in-plane resolution = 0.27 mm, slice thickness/gap = 0.5 mm, 248 slices).

Image co-registration

In each study, structural MRI scans were used to ensure accurate co-registration of the FDG-PET images. Structural MRI images were aligned to a rhesus monkey MRI template based on 592 young animals described in Fox *et al.* (2015) (16) using ANTS (pure cross correlation with a window radius of 2 and a weight of 1, with a Gaussian kernel with sigma 2 applied to the similarity gradient, with a SyN transformation model, and 30x20x20x5 iterations). Rigid body registration was used to align the FDG-PET from each animal to the corresponding structural MRI image with a mutual information algorithm using ANTS. Once the FDG-PET and T1-MRI were in the same space, the nonlinear transformation based on the T1-MRI was applied to produce FDG-PET images in standard space.

Tissue processing and RNA extraction

After the animal was euthanized, the brain was removed and placed in a brain block. Tissue was cut into slabs as previously described (17) and frozen by immediate submersion in dry ice-chilled isopentane. Tissue slabs were stored at -80°C until use. On the day of dissection, the appropriate slab was slightly thawed on wet ice and then the dorsal amygdala was collected using a circular 3 mm punch tool as previously described (17). RNA was extracted from the tissue punches using RNeasy plus mini kits (Qiagen, Germantown, MD) and processed for RNA-seq library construction.

RNA-seq library construction

RNA-Seq was performed using a modification of the SPIA reaction of the NuGEN Ovation RNaseq V2 kit for cDNA Synthesis, followed by library construction using the NuGEN Rapid no-PCR protocol in a NuGEN Mondrian microfluidics instrument. This method uses linear amplification and amplifies the nucleic acid ~1,000X by the end of library construction. Additionally, the method uses random primers for cDNA synthesis and hence assays non-polyA non-coding RNAs, and can provide near perfect 5'→3' read distribution (18). RNA-Seq libraries were then sequenced to a minimum depth of ~30 million single-end 101 base-pair reads. Replicates of 1ng (~100 cell equivalents) of Universal Human Reference (UHR) RNA (Agilent Technologies Inc., 740000) sequenced using this method had an average pairwise r^2 of 0.92 (18).

Trajectory guide base placement and intraoperative MRI (IMRI)

Placement of the MRI-compatible trajectory guide bases followed previously reported methods (19, 20) modified for targeting dorsal amygdala, and are described in detail in the Supplemental Information accompanying Kalin et al. (2016) (21). The intraoperative targeting was performed using a platform for real-time MR-guided prospective stereotaxy (22) that was initially developed by the University of Wisconsin (23-26). To cover as much of the dorsal amygdala as possible while minimizing treatment to surrounding regions, two 6 μ l infusions were performed per hemisphere (one anterior target, one posterior target), for a total of 12 μ l per hemisphere. After each infusion the catheter was removed, and after all infusions were complete the animal was transported back to the surgical suite and the craniotomies were closed.

Before the procedure, the animals were anesthetized with ketamine (up to 20 mg/kg, intramuscular (IM)), prepared for surgery, and then placed in a MRI compatible-stereotaxic frame. The animals were intubated and received isoflurane anesthesia (1–3%, intratracheal (IT)). Atropine sulfate (0.01-0.3 mg/kg, IM) was administered to depress salivary secretion, and buprenorphine (0.01-0.03 mg/kg, IM, repeated every 6-12 hours) was given for analgesia. To maintain fluids and electrolytes, Plasmalyte (up to 10 mg/kg/hr, intravenous (IV)) was administered. Cefazolin (20-25 mg/kg, IM or IV) was administered as a prophylactic antibiotic one day prior to the surgery. Cefazolin was also administered immediately prior to surgery, and then every 6 hours while under anesthesia. All drugs and treatments were given in consultation with veterinary staff. Vital signs (heart rate, respiration, oxygen saturation, and end tidal CO₂) were

continuously monitored. Body temperature was monitored during the surgical procedure and maintained by wrapping the animals for warmth.

Prior to surgery the 3D T1W MRIs were used to visualize target in three planes (sagittal, axial, and coronal) and identify the entry point for the catheter. Intraoperative MRI guidance of the catheter was performed using a pivot point-based MRI compatible external trajectory guide (Navigus™ brain port, Medtronic Inc., Minneapolis, MN). Modifications were made to this system to adapt it for the placement of catheters by the addition of a guiding insert, a customized base to fit the nonhuman primate skull and the addition of a laser alignment pointer that fastens to a micromanipulator. Placement of the MRI-compatible trajectory guide bases was performed in a surgical suite under sterile conditions. Using stereotactic guidance, 11-12 mm in diameter craniotomies were made bilaterally at the planned entry points. Each trajectory guide base was mounted on the skull over the craniotomy with three titanium AutoDrive self-tapping screws (OsteoMed, Addison, TX) and dental acrylic. Surgical gelfoam that was moistened with sterile saline was placed over the craniotomies and the bases were capped with sterile plastic base plugs (Navigus).

Catheter trajectory planning and insertion

The animals were transported from the surgical suite to the MRI suite under anesthesia. Sterile conditions were maintained in the MRI suite during viral vector delivery. A 3-inch circular surface coil (MR Instruments, Minneapolis, MN) was positioned above the animal's head, transverse to the main magnetic field, with the Navigus brain port located near the center of the coil. A sterile

MR-visible alignment guide was inserted into the trajectory guide base. The base constrains the guide such that its proximal tip passes the center of the pivot joint, and the distal end of the guide extends away from the skull. A high-resolution, volumetric roadmap scan was acquired for target identification using a 3D IR GRE MRI scan. After identifying the desired target point in the brain and the location of the pivot point in the high-resolution 3D T1-weighted “roadmap” volume, the prospective stereotaxy tool calculates an “aiming point” outside the skull that is collinear with the target and alignment guide pivot points and then performs real-time imaging of a plane perpendicular to and centered on the aiming point, allowing the operator to reach into the bore of the magnet and move the alignment guide until its image overlaps with the software-displayed aiming point. This system is built on top of the RTHawk scanner interface (HeartVista, Palo Alto, CA), which permits the implementation of image-guided interventional procedures (27), and the VURTIGO toolkit (Visual Understanding of Real-Time Image Guided Operations, Sunnybrook Health Sciences Centre; Toronto, Canada), an open-source visualization platform that allows simultaneous display and interaction with multiple 3D and 2D datasets (28).

Once the alignment guide was determined to be in position, the base was locked into place, the fluid-filled alignment guide was removed, the remote introducer (Navigus) was fastened to the stem, and a catheter guiding insert was placed in the alignment stem. The catheter for the infusion was threaded through the remote introducer and the guiding insert, and was fastened to the remote introducer by a plastic locking mechanism. FEP Teflon infusion lines (IDEX Health & Science, Oak Harbor, WA) were used to connect the catheter via a pressure sensor transducer to a 100 microliter (μ l) Hamilton syringe (Hamilton Company USA, Reno, NV) that was placed in

a MRI-compatible syringe pump attached to the control mechanism of a standard Harvard apparatus PHD 2000 (Holliston, MA). Monitoring of the pressure in the infusion line was performed using the infusion pump controller system (Engineering Resources Group, Inc., Pembroke Pines, FL). A computer was connected to the pump controller for infusion protocol programming, which was connected to a pressure sensor transducer to monitor infusion line pressure at the pump output port. The infusion line was primed with a loading line solution (Dulbecco's phosphate-buffered saline (D-PBS) without Ca^{2+} and Mg^{2+} with 5% glycerol) and the catheter was loaded with the viral vector containing the NT3 construct and the MR visible marker Gadobenate dimeglumine (Gd, MultiHance, Bracco Diagnostics).

The catheter (100mm Valve Tip Catheter, Engineering Resources Group, Inc., Pembroke Pines, FL) was a fused silica cannula with a polyimide tubing tip and was sealed with a retractable glass fiber stylet. Its dimensions were: tip—outer diameter (OD)=0.40 mm, inner diameter (ID)=0.345 mm, length = 3.0 mm; shaft—OD = 0.67 mm, ID = 0.45 mm, length = 97.0 mm from ferrule, stylet OD = 0.275 mm.

After pressure in the line was stabilized, the catheter was introduced into the brain, advancing the remote introducer at approximately 10-15 mm/minute. The catheter was advanced two-thirds of the measured depth towards the target for partial insertion, and another targeting 3D T1W MRI was performed to confirm the correct trajectory, and calculate the remaining distance from catheter tip to target. Once confirmed, the catheter was advanced to its final position and

the stylet was retracted. When the pressure reading on the infusion pump controller system stabilized, the infusion began.

The infusate consisted of AAV5-NT3 vector in a solution of D-PBS without Ca^{2+} and Mg^{2+} with 5 % glycerol. To facilitate *in vivo* MRI visualization of the infusion, Gd was mixed with the viral vector to reach final concentration 0.66 mM. A total volume of 6 μl was infused at a steady rate of 1 $\mu\text{l}/\text{min}$ per infusion site, for a total of 12 μl per hemisphere. After each infusion the previously described 3D roadmap scan was reacquired for a qualitative visualization of the volumetric infusate delivery region. This sequence provides sensitivity to the contrast-enhanced infusate and sufficient gray/white contrast for easy identification of the infusion's anatomical location. These post infusion scans were used to create the infusion overlap image in Figure 3e in the main manuscript. After all infusions were complete the animal was transported back to the surgical suite. To reduce intracranial pressure and prevent brain swelling, Mannitol (up to 2.0 g/kg, IV) was given as needed. The brain ports were removed and the incision was closed in layers before the animal was allowed to recover from anesthesia. Animals were given buprenorphine twice on the day following the surgery (0.01-0.03 mg/kg, IM). Cefazolin (20-25 mg/kg, IM or IV) or Cephalexin (20-25 mg/kg, oral (PO)) was given twice daily for five days after surgery to prevent infection. The animals were allowed to recover and testing did not commence before 2 months after surgery.

AAV construction

The DNA sequence corresponding to the entire open reading frame of the rhesus NTF3 (GenBank accession #XM_001118191, bases 8 to 1033) was inserted into the viral vector pAAV-MCS (Vector Biolabs, Malvern, PA). Expression of the NTF3 was under control of the CMV promoter, and successful plasmid-driven expression of NTF3 was first confirmed *in vitro* by transfecting HEK293 cells grown on glass coverslips. Forty-eight hours after transfection, the cells were fixed at 4°C with 4% paraformaldehyde for four days, followed by two 2 min washes with phosphate-buffered saline (PBS). The expression of NTF3 in the HEK293 cells was shown by fluorescent immunocytochemistry. First, cells were permeabilized with a 5 min incubation with 0.25% Triton X-100 (Sigma-Aldrich, St Louis, MO) in PBS followed by two 2 min washes with PBS and then non-specific binding was blocked for one hour with 5% normal donkey serum (Jackson ImmunoResearch, West Grove, PA) in PBS. All subsequent incubation steps were performed in PBS containing 5% normal donkey serum. NTF3 expression was detected using an overnight incubation at 4°C with a 1:80 dilution of an antigen affinity-purified anti-human NTF3 polyclonal antibody raised in goat (R&D Systems, Minneapolis, MN). Following four 10 min washes with PBS containing 5% normal donkey serum, the cells were incubated at room temperature for two hours with a 1:200 dilution of Alexa Fluor 488 conjugated donkey anti-goat secondary antibody (ThermoFisher Scientific, Waltham, MA). After four 10 min washes with PBS, coverslips were mounted on Superfrost Plus slides with ProLong Gold (ThermoFisher Scientific). Fluorescence was visualized using a DMI6000B microscope (Leica Microsystems, Buffalo Grove, IL). Following confirmation of NTF3 protein expression, the plasmid was then packaged into rAAV5 (Vector Biolabs) with a titer of 1.2×10^{13} genome copies/ml.

NTF3 immunohistochemistry

Animals were euthanized by transcardial perfusion with heparinized PBS at room temperature followed by fixation with 4% paraformaldehyde (PFA) at 4°C. Brains were removed and PFA fixation was continued overnight at 4°C. The brains were placed in a brain block and cut into slabs that were subsequently processed through increasing concentrations of sucrose – 10%, 20% and 30%. The approximately 14 mm thick tissue slab containing the amygdala was frozen and cut at 40 microns on a cryostat (CryoStar NX50, ThermoFisher Scientific). Tissue sections were stored in cryoprotectant (40 mM potassium phosphate/11mM sodium phosphate buffer, pH 7.2, containing 30% ethylene glycol and 30% sucrose) at -20°C until use. To identify neurons that expressed NTF3, immunofluorescence was performed. Cryoprotectant was removed by washing sections for 5 hours with PBS; then non-specific binding was blocked for one hour with 5% normal donkey serum (Jackson ImmunoResearch). This, and all subsequent incubation steps were carried out at room temperature in PBS containing 0.3% Triton X-100 (Sigma-Aldrich, St Louis, MO). After each incubation step, sections received three 10 min washes with PBS. Neurons were identified using an overnight incubation with a 1:2000 dilution of a mouse monoclonal neuronal nuclei (NeuN) antibody (clone A60; MilliporeSigma, Burlington, MA) followed by a one-hour incubation with a 1:250 dilution of Alexa Fluor 647 conjugated donkey anti-mouse secondary antibody (ThermoFisher Scientific). NTF3 expressing cells were then identified using an overnight incubation with a 1:200 dilution of the same R&D systems NTF3 antibody used for the *in vitro* studies described in the preceding paragraph followed by a one-hour incubation with a 1:250 dilution of Alexa Fluor 488 conjugated donkey anti-goat secondary antibody (ThermoFisher Scientific). Finally, cellular nuclei were identified using a 5 min incubation with a 1:5000 dilution

of 4',6-diamidino-2-phenylindole (DAPI). Sections were mounted on Superfrost Plus microscope slides using ProLong Gold. Fluorescence was visualized using an oil emersion 40x object with 1.3 na on an A1R-SI+ confocal microscope (Nikon Instruments, Melville, NY).

RNA-seq alignment and quantification

RNA-seq reads were aligned to the Rhesus genome (MaSuRCA v7) using PerM as described in RseqFlow (29). In short, Reads were iteratively aligned with full sensitivity to eight mismatches to coding exons, coding junctions, introns and intergenic regions according to the Rhesus transcriptome (UNMC v7.6.8). Reads which aligned to coding exons and known junctions in each gene model were summed to provide a raw proxy for gene expression. The number of reads per gene in each animal was normalized both by the rank distribution (quantile) as well as by total number of gene-aligned reads (rpkm).

To provide a more in-depth exploration of isoform expression we described the expression per “feature” where features refer to each unique exon or exon-exon junction in a gene model. While specific isoform level expression requires complete knowledge of the set of exons specific to each isoform in a gene model, analysis of features allows each feature to be independently investigated for its association with anxious temperament.

RNA-seq across subject analyses

Analyses were performed to assess the relationship between gene expression and AT in python using statsmodels (<https://github.com/statsmodels/statsmodels/>). Because annotation of the

rhesus genome is ongoing, and our understanding of splice variation still developing, we performed gene-level multiple regression analyses to predict AT. Each multiple regression analysis was performed in two steps, 1) nuisance variable age was entered into the model to predict AT, 2) estimated expression levels for each exon were simultaneously entered. The test of interest was the significance of the F-change between step 1 and step 2, which accounts for the variance explained by the exonic expression levels. The degrees of freedom for this model vary depending on the number of exons expressed for each gene. Analyses were restricted to genes where we mapped an average of at least 10 reads across subjects, and at least one read in each animal.

In addition to this primary analysis, we performed a series of non-independent follow-up analyses. These analyses included performing independent regressions to predict AT for each gene, and each annotated feature of the rhesus genome, while controlling for age. These analyses are for exploratory purposes only, as we did not correct for multiple comparisons or account for non-independence. All analyses performed can be examined via our web-resource. Follow-up analyses were performed in relation to NTRK3 expression levels, specifically, using non-parametric spearman's correlations between each gene feature and AT. Ontology analyses were performed in reference to the human genome using the Enrichr tool (30, 31).

Voxelwise FDG-PET across subject analyses

Across subject FDG-PET analyses were performed using fmristat in MATLAB, similar to published reports (see: (8, 11, 16)). Voxelwise regressions were performed to examine the relationship

between FDG-PET metabolism in the NEC context and AT, while controlling for age. Results were thresholded at $p < .005$, two-tailed uncorrected. To examine the extent to which FDG-AT relationships were representative of our previously published large-scale analysis of the neural correlates of AT, we examined the spatial correlation between the FDG-AT voxelwise map in these animals and the previously reported FDG-AT voxelwise map in a sample of 592 young rhesus monkeys (16).

To identify regions where FDG-PET was associated with dorsal amygdala gene expression, we performed voxelwise correlations between FDG and dorsal amygdala gene expression levels in 46 animals. Because this analysis can provide an unreasonable set of data, we restricted our analysis to a few features of interest (RPS6KA4, NTRK3, GABAR5, PENK, APP, ADRA2C, and HRH1). To get a less computationally intensive overview of the relationship between AT-related metabolism and dorsal amygdala gene expression in other transcripts, we used a region of interest approach. More specifically, we extracted mean metabolism within the AT-related cluster (Table S1), and used the feature-based multiple regression approach described above to predict mean metabolism in each significant region. Results are available on our web-resource (<http://at.psychiatry.wisc.edu>; https://github.com/asfox/AT_DorsalAmygdala_RNAseq_FoxEtAl).

AAV-NT3 statistical analyses

Changes between pre- and post-surgical measures of AT were computed for the dorsal amygdala AAV5-NTF3 animals and compared to similarly-spaced assessments of the control animals.

Corresponding comparisons were also performed to assess the effects of dorsal amygdala AAV5-NTF3 on the components of AT, i.e. freezing, cooing, and cortisol levels. The effects of NTF3 overexpression were assessed using the statsmodels package in python (<https://github.com/statsmodels/statsmodels/>).

To assess the effects of dorsal amygdala AAV5-NTF3 on brain metabolism in the infused region, we identified voxels that received infusate (as measured by intra-operative Gd), and examined the relationship between the number of subjects that received infusate in that voxel and the group-difference in metabolic change compared to controls. This analysis identified regions infusion-overlap related group-differences in NEC-context metabolism, such that the infusion-induced metabolic changes were larger in those voxels in which more subjects received infusate (Figure 3e). The effects of NTF3 overexpression on metabolism in the infused region were assessed using the statsmodels package in python (<https://github.com/statsmodels/statsmodels/>).

Voxelwise analyses to examine the broader effects of NTF3 overexpression on brain metabolism were performed using the fmristat packages in MATLAB, as above (also see: (21)). We first computed the changes in metabolism pre- and post-surgery, and similarly timed assessments in control animals. We then performed group t-tests to compare changes in metabolism between groups. Because these analyses were exploratory, results were thresholded at a liberal $p < .05$ two tailed, uncorrected.

Code availability

All code used for RNA-seq alignment is available by contacting T Souaiaia (tade.souaiaia@gmail.com). All code used for neuroimaging and across subject statistics is available by contacting AS Fox (dfox@ucdavis.edu).

Data availability

All data is publicly available. Raw RNA-seq reads from the dorsal amygdala region of nonhuman primates can be found on NCBI (uploaded upon acceptance). All RNA-seq analyses are available online via our web-resource (<http://at.psychiatry.wisc.edu>; or from github: https://github.com/asfox/AT_DorsalAmygdala_RNAseq_FoxEtAl). Voxelwise PET analyses can be found on Neurovault (<https://www.neurovault.org/collections/AYJGSCJH/>). Raw data available upon request from NH Kalin (nkalin@wisc.edu).

Supplementary Figures

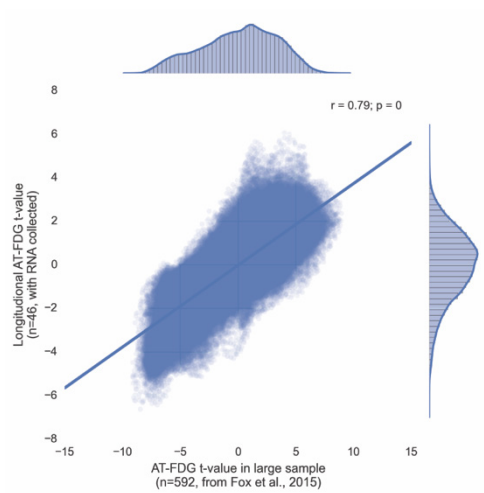


Figure S1: *The spatial distribution of the AT-FDG relationship in these 46 animals was spatially correlated with the distribution of AT-FDG in our previously published large sample of 592 rhesus monkeys. To identify the regions of the brain where metabolism was associated with AT we performed voxelwise correlations between AT and FDG-PET measures of metabolism during NEC. The histograms and scatter plot for the spatial correlation between these two AT-FDG is seen above.*

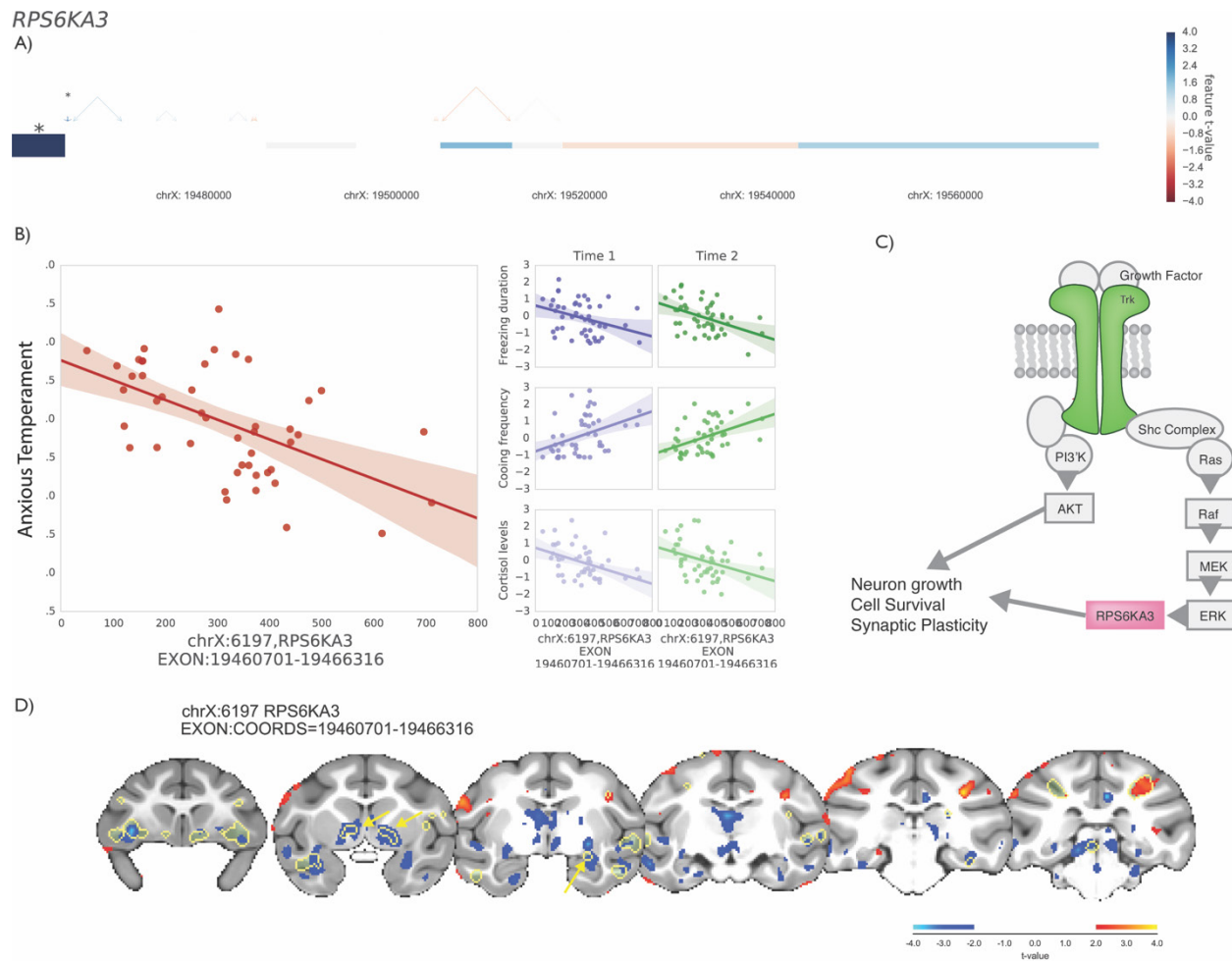


Figure S2: Expression of RPS6KA3, a downstream effector of growth factor receptors, was associated with AT, and its components (n=46). The working gene model for RPS6KA3 (a) with significant regions colored by the t-value of their relationship with AT (a, color-bar). The scatter plots between the most significant exon and anxious temperament (b, left, red scatterplot) as well as for the components of AT (right scatterplots), freezing (top), cooing (middle) and cortisol (bottom) for both time 1 (blue) and time 2 (green). RPS6KA3 is proposed to play a role in tyrosine receptor kinase growth signaling via the MEK-ERK pathway (c). Expression of the most significant RPS6KA3 exon is associated with FDG-PET metabolism (d) throughout the AT-network, as defined by AT-related metabolism from Figure 1 (d; yellow outline), including the dorsal amygdala and bed nucleus of the stria terminalis (yellow arrows). A full un-thresholded voxelwise map can be found on Neurovault.org at: <https://www.neurovault.org/collections/AYJGSCJH>.

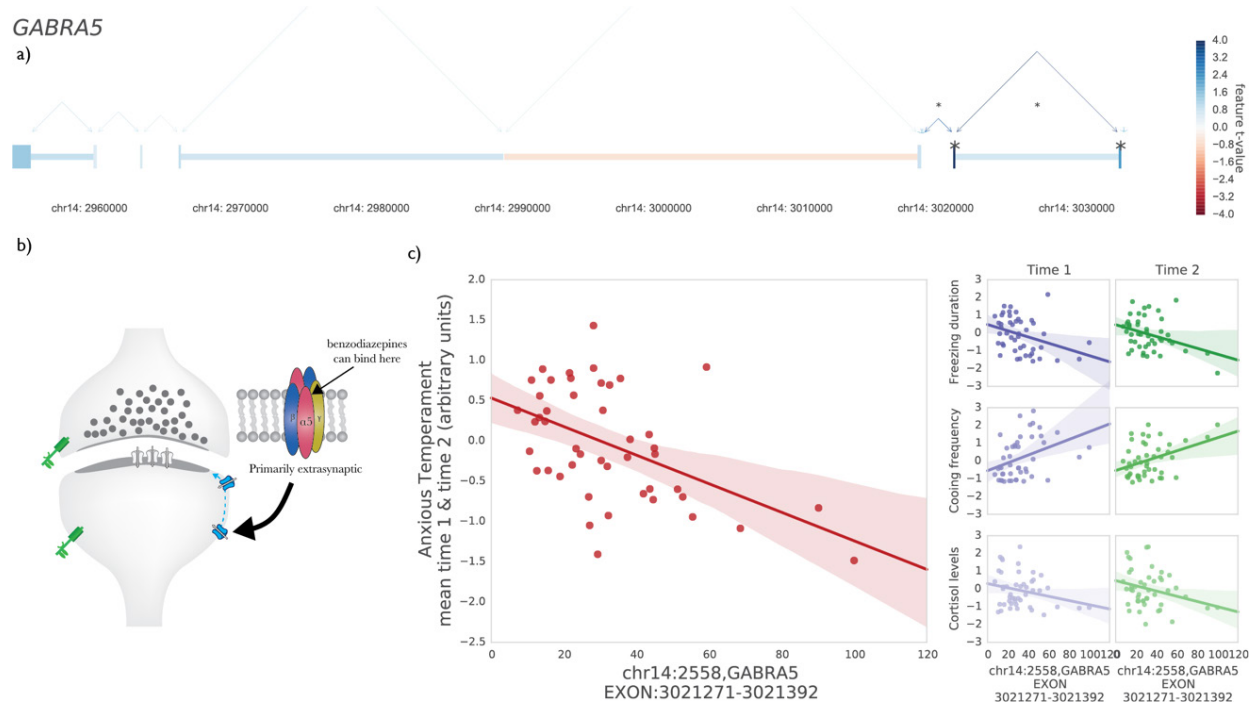


Figure S3: Expression of GABRA5, a GABA-receptor component, was inversely associated with AT, and its components (n=46). The working gene model for GABRA5 (a) with significant regions colored by the t-value of their relationship with AT (a, color-bar). The GABRA5 subunit is primarily expressed on extrasynaptic GABA-receptors in the dorsal amygdala (b, schematic). The scatter plots between the most significant exon and anxious temperament (c, left, red scatterplot) as well as for the components of AT (right scatterplots), freezing (top), cooling (middle) and cortisol (bottom) for both time 1 (blue) and time 2 (green).

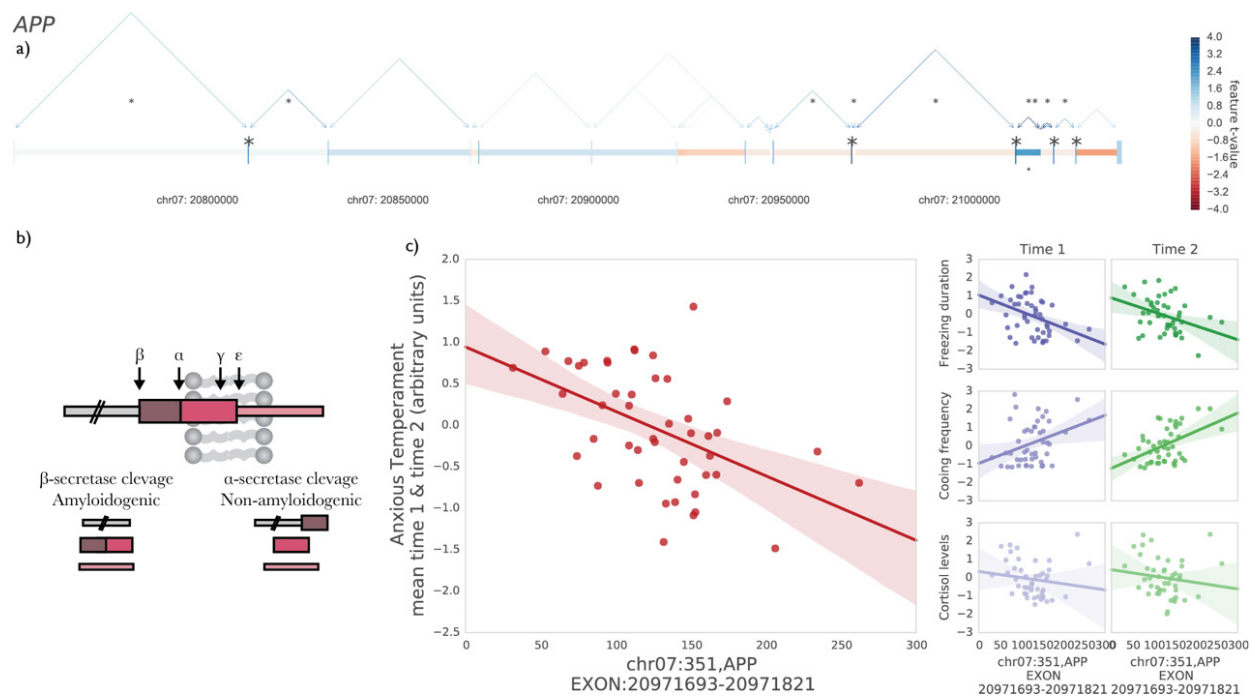


Figure S4: Expression of APP, a gene typically associated with Alzheimer's, was inversely associated with AT, and its components (n=46). The working gene model for APP (a) with significant regions colored by the t-value of their relationship with AT (a, color-bar). The AT-related APP gene features were primarily located near the α/β -secretase cleavage sites (b, schematic). The scatter plots between the most significant exon and anxious temperament (c, left, red scatterplot), as well as for the components of AT (right scatterplots), freezing (top), cooling (middle) and cortisol (bottom) for both time 1 (blue) and time 2 (green).

Supplemental References

1. Dawkins E, Small DH (2014): Insights into the physiological function of the beta-amyloid precursor protein: beyond Alzheimer's disease. *J Neurochem.* 129:756-769.
2. Tasan RO, Bukovac A, Peterschmitt YN, Sartori SB, Landgraf R, Singewald N, et al. (2011): Altered GABA transmission in a mouse model of increased trait anxiety. *Neuroscience.* 183:71-80.
3. Heldt SA, Ressler KJ (2007): Training-induced changes in the expression of GABAA-associated genes in the amygdala after the acquisition and extinction of Pavlovian fear. *Eur J Neurosci.* 26:3631-3644.
4. Clement Y, Prut L, Saurini F, Mineur YS, Le Guisquet AM, Vedrine S, et al. (2012): Gabra5-gene haplotype block associated with behavioral properties of the full agonist benzodiazepine chlordiazepoxide. *Behav Brain Res.* 233:474-482.
5. Botta P, Demmou L, Kasugai Y, Markovic M, Xu C, Fadok JP, et al. (2015): Regulating anxiety with extrasynaptic inhibition. *Nat Neurosci.* 18:1493-1500.
6. O'Brien RJ, Wong PC (2011): Amyloid precursor protein processing and Alzheimer's disease. *Annu Rev Neurosci.* 34:185-204.
7. Kamenetz F, Tomita T, Hsieh H, Seabrook G, Borchelt D, Iwatsubo T, et al. (2003): APP processing and synaptic function. *Neuron.* 37:925-937.
8. Fox AS, Shelton SE, Oakes TR, Davidson RJ, Kalin NH (2008): Trait-like brain activity during adolescence predicts anxious temperament in primates. *PLoS ONE.* 3:e2570.
9. Kalin NH (1993): The neurobiology of fear. *Sci Am.* 268:94-101.
10. Kalin NH, Shelton SE (1989): Defensive behaviors in infant rhesus monkeys: environmental cues and neurochemical regulation. *Science.* 243:1718-1721.
11. Oler JA, Fox AS, Shelton SE, Rogers J, Dyer TD, Davidson RJ, et al. (2010): Amygdalar and hippocampal substrates of anxious temperament differ in their heritability. *Nature.* 466:864-868.
12. Shackman AJ, Fox AS, Oler JA, Shelton SE, Davidson RJ, Kalin NH (2013): Neural mechanisms underlying heterogeneity in the presentation of anxious temperament. *Proceedings of the National Academy of Sciences of the United States of America.* 110:6145-6150.

13. Fox AS, Kalin NH (2014): A Translational Neuroscience Approach to Understanding the Development of Social Anxiety Disorder and Its Pathophysiology. *The American journal of psychiatry*.
14. Avants BB, Tustison NJ, Song G, Cook PA, Klein A, Gee JC (2011): A reproducible evaluation of ANTs similarity metric performance in brain image registration. *NeuroImage*. 54:2033-2044.
15. Avants BB, Yushkevich P, Pluta J, Minkoff D, Korczykowski M, Detre J, et al. (2010): The optimal template effect in hippocampus studies of diseased populations. *NeuroImage*. 49:2457-2466.
16. Fox AS, Oler JA, Shackman AJ, Shelton SE, Raveendran M, McKay DR, et al. (2015): Intergenerational neural mediators of early-life anxious temperament. *Proc Natl Acad Sci U S A*. 112:9118-9122.
17. Fox AS, Oler JA, Shelton SE, Nanda SA, Davidson RJ, Roseboom PH, et al. (2012): Central amygdala nucleus (Ce) gene expression linked to increased trait-like Ce metabolism and anxious temperament in young primates. *Proc Natl Acad Sci U S A*. 109:18108-18113.
18. Dueck HR, Ai R, Camarena A, Ding B, Dominguez R, Evgrafov OV, et al. (2016): Assessing characteristics of RNA amplification methods for single cell RNA sequencing. *BMC Genomics*. 17:966.
19. Emborg ME, Hurley SA, Joers V, Tromp do PM, Swanson CR, Ohshima-Hosoyama S, et al. (2014): Titer and product affect the distribution of gene expression after intraputamenal convection-enhanced delivery. *Stereotact Funct Neurosurg*. 92:182-194.
20. Emborg ME, Joers V, Fisher R, Brunner K, Carter V, Ross C, et al. (2010): Intraoperative intracerebral MRI-guided navigation for accurate targeting in nonhuman primates. *Cell transplantation*. 19:1587-1597.
21. Kalin NH, Fox AS, Kovner R, Riedel MK, Fekete EM, Roseboom PH, et al. (2016): Overexpressing Corticotropin-Releasing Hormone in the Primate Amygdala Increases Anxious Temperament and Alters Its Neural Circuit. *Biol Psychiatry*.
22. Truwit CL, Liu H (2001): Prospective stereotaxy: a novel method of trajectory alignment using real-time image guidance. *Journal of magnetic resonance imaging : JMRI*. 13:452-457.
23. Brodsky EK, Block WF, Alexander AL, Emborg ME, Ross CD, Sillay KA (2011): Intraoperative device targeting using real-time MRI. *Biomedical Sciences and Engineering Conference (BSEC), 2011*, pp 1-4.

24. Grabow B, Block W, Alexander AL, Hurley S, CD R, Sillay K, et al. (2012): Extensible real-time MRI platform for intraoperative targeting and monitoring. *ISMRM Nineteenth Annual Scientific Meeting and Exhibition, poster presentation #1585*. Melbourne, Australia.
25. Grabow BP, Oler JA, Riedel M, Fekete EM, Kovner R, brodsky EK, et al. (2014): Alteration of Molecular Neurochemistry: MRI-guided Delivery of Viral Vectors to the Primate Amygdala. *ISMRM Twenty-First Annual Scientific Meeting and Exhibition, oral presentation #672*. Milan, Italy.
26. Brady ML, Raghavan R, Block W, Grabow B, Ross C, Kubota K, et al. (2015): The Relation between Catheter Occlusion and Backflow during Intraparenchymal Cerebral Infusions. *Stereotact Funct Neurosurg*. 93:102-109.
27. Santos JM, Wright GA, Pauly JM (2004): Flexible Real-Time Magnetic Resonance Imaging Framework.1048-1051.
28. Radau PE, Pintilie S, Flor R, Biswas L, Oduneye SO, Ramanan V, et al. (2012): VURTIGO : Visualization Platform for Real-Time , MRI-Guided Cardiac Electroanatomic Mapping.244-253.
29. Wang Y, Mehta G, Mayani R, Lu J, Souzaiaia T, Chen Y, et al. (2011): RseqFlow: workflows for RNA-Seq data analysis. *Bioinformatics*. 27:2598-2600.
30. Chen EY, Tan CM, Kou Y, Duan Q, Wang Z, Meirelles GV, et al. (2013): Enrichr: interactive and collaborative HTML5 gene list enrichment analysis tool. *BMC Bioinformatics*. 14:128.
31. Kuleshov MV, Jones MR, Rouillard AD, Fernandez NF, Duan Q, Wang Z, et al. (2016): Enrichr: a comprehensive gene set enrichment analysis web server 2016 update. *Nucleic Acids Res*. 44:W90-97.